

# Initial operations of the Soft X-ray Imager onboard XRISM

Hiromasa Suzuki<sup>a</sup>, Tomokage Yoneyama<sup>b</sup>, Shogo B. Kobayashi<sup>c</sup>, Hirofumi Noda<sup>d</sup>, Hiroyuki Uchida<sup>e</sup>, Kumiko K. Nobukawa<sup>f</sup>, Kouichi Hagino<sup>g</sup>, Koji Mori<sup>h</sup>, Hiroshi Tomida<sup>a</sup>, Hiroshi Nakajima<sup>i</sup>, Takaaki Tanaka<sup>j</sup>, Hiroshi Murakami<sup>k</sup>, Hideki Uchiyama<sup>l</sup>, Masayoshi Nobukawa<sup>m</sup>, Yoshiaki Kanemaru<sup>a</sup>, Yoshinori Otsuka<sup>h</sup>, Haruhiko Yokosu<sup>h</sup>, Wakana Yonemaru<sup>h</sup>, Hanako Nakano<sup>h</sup>, Kazuhiro Ichikawa<sup>h</sup>, Reo Takemoto<sup>h</sup>, Tsukasa Matsushima<sup>h</sup>, Marina Yoshimoto<sup>n</sup>, Mio Aoyagi<sup>n</sup>, Kohei Shima<sup>n</sup>, Yuma Aoki<sup>f</sup>, Yamato Ito<sup>f</sup>, Kaito Fukuda<sup>f</sup>, Honoka Kiyama<sup>f</sup>, Daiki Aoki<sup>o</sup>, Kaito Fujisawa<sup>o</sup>, Yasuyuki Shimizu<sup>o</sup>, Mayu Higuchi<sup>o</sup>, Masahiro Fukuda<sup>i</sup>, Natsuki Sakamoto<sup>p</sup>, Ryuichi Azuma<sup>j</sup>, Shun Inoue<sup>e</sup>, Takayoshi Kohmura<sup>o</sup>, Makoto Yamauchi<sup>h</sup>, Isamu Hatsukade<sup>h</sup>, Hironori Matsumoto<sup>n</sup>, Hirokazu Odaka<sup>n</sup>, Tsunefumi Mizuno<sup>p</sup>, Tessei Yoshida<sup>a</sup>, Yoshitomo Maeda<sup>a</sup>, Manabu Ishida<sup>a</sup>, Takeshi G. Tsuru<sup>e</sup>, Kazutaka Yamaoka<sup>q</sup>, Takashi Okajima<sup>r</sup>, Takayuki Hayashi<sup>r,u</sup>, Junko S. Hiraga<sup>s</sup>, Masanobu Ozaki<sup>t</sup>, Tadayasu Dotani<sup>a,v</sup>, Hiroshi Tsunemi<sup>n</sup>, and Kiyoshi Hayashida<sup>n</sup>

<sup>a</sup>Japan Aerospace Exploration Agency, Institute of Space and Astronautical Science, 3-1-1 Yoshino-dai, Chuo-ku, Sagami-hara, Kanagawa 252-5210, Japan

<sup>b</sup>Faculty of Science and Engineering, Chuo University, 1-13-27 Kasuga, Bunkyo, Tokyo 112-8551, Japan

<sup>c</sup>Department of Physics, Faculty of Science, Tokyo University of Science, Kagurazaka, Shinjuku-ku, Tokyo 162-0815, Japan

<sup>d</sup>Astronomical Institute, Tohoku University, 6-3 Aramaki-zaaoba, Aoba-ku, Sendai, Miyagi 980-8578, Japan

<sup>e</sup>Department of Physics, Kyoto University, Kitashirakawa Oiwake-cho, Sakyo-ku, Kyoto, Kyoto 606-8502, Japan

<sup>f</sup>Department of Physics, Kindai University, 3-4-1 Kowakae, Higashi-Osaka, Osaka 577-8502, Japan

<sup>g</sup>Department of Physics, University of Tokyo, 7-3-1 Hongo, Bunkyo, Tokyo 113-0033, Japan

<sup>h</sup>Faculty of Engineering, University of Miyazaki, 1-1 Gakuen Kibanadai Nishi, Miyazaki, Miyazaki 889-2192, Japan

<sup>i</sup>College of Science and Engineering, Kanto Gakuin University, Kanazawa-ku, Yokohama, Kanagawa 236-8501, Japan

<sup>j</sup>Department of Physics, Konan University, 8-9-1 Okamoto, Higashinada, Kobe, Hyogo 658-8501, Japan

<sup>k</sup>Faculty of Informatics, Tohoku Gakuin University, 3-1 Shimizukoji, Wakabayashi-ku, Sendai, Miyagi 984-8588, Japan

<sup>l</sup>Science Education, Faculty of Education, Shizuoka University, Suruga-ku, Shizuoka, Shizuoka 422-8529, Japan

<sup>m</sup>Faculty of Education, Nara University of Education, Nara, Nara 630-8528, Japan

<sup>n</sup>Department of Earth and Space Science, Osaka University, 1-1 Machikaneyama-cho, Toyonaka, Osaka 560-0043, Japan

<sup>o</sup>Department of Physics, Faculty of Science and Technology, Tokyo University of Science, 2641 Yamazaki, Noda, Chiba 270-8510, Japan

<sup>p</sup>Hiroshima Astrophysical Science Center, Hiroshima University, 1-3-1 Kagamiyama, Higashi-Hiroshima, Hiroshima 739-8526, Japan

<sup>q</sup>Department of Physics, Nagoya University, Chikusa-ku, Nagoya, Aichi 464-8602, Japan

<sup>r</sup>NASA’s Goddard Space Flight Center, Greenbelt, MD 20771, USA

<sup>s</sup>Department of Physics, Kwansei Gakuin University, 2-2 Gakuen, Sanda, Hyogo 669-1337, Japan

<sup>t</sup>Advanced Technology Center, National Astronomical Observatory of Japan, Mitaka, Tokyo 181-8588, Japan

<sup>u</sup>Center for Space Science and Technology, University of Maryland, Baltimore County (UMBC), Baltimore, MD 21250, USA

<sup>v</sup>Department of Space and Astronautical Science, School of Physical Sciences, SOKENDAI (The Graduate University for Advanced Studies), 3-1-1 Yoshino-dai, Chuou-Ku, Sagamihara, Kanagawa 252-5210, Japan

## ABSTRACT

XRISM (X-Ray Imaging and Spectroscopy Mission) is an astronomical satellite with the capability of high-resolution spectroscopy with the X-ray microcalorimeter, Resolve, and wide field-of-view imaging with the CCD camera, Xtend. The Xtend consists of the mirror assembly (XMA: X-ray Mirror Assembly) and detector (SXI: Soft X-ray Imager). The components of SXI include CCDs, analog and digital electronics, and a mechanical cooler. After the successful launch on September 6th, 2023 (UT) and subsequent critical operations, the mission instruments were turned on and set up. The CCDs have been kept at the designed operating temperature of  $-110^{\circ}\text{C}$  after the electronics and cooling system were successfully set up. During the initial operation phase, which continued for more than a month after the critical operations, we verified the observation procedure, stability of the cooling system, all the observation options with different imaging areas and/or timing resolutions, and operations for protection against South Atlantic Anomaly. We optimized the operation procedure and observation parameters including the cooler settings, imaging areas for the specific modes with higher timing resolutions, and event selection algorithm. We summarize our policy and procedure of the initial operations for SXI. We also report on a couple of issues we faced during the initial operations and lessons learned from them.

**Keywords:** X-rays, X-ray astronomy, XRISM, Xtend, SXI, X-ray CCD

## 1. INTRODUCTION: SOFT X-RAY IMAGER (SXI) ONBOARD XRISM

X-Ray Imaging and Spectroscopy Mission (XRISM)<sup>1–3</sup> is the Japan’s 7th X-ray astronomical satellite mission, which is equipped with the microcalorimeter “Resolve”<sup>4</sup> and large field-of-view CCD camera “Xtend”<sup>5–7</sup> in combination with the X-ray mirror assemblies.<sup>8,9</sup> XRISM was successfully launched into a low-earth orbit on September 6th, 2023 (UT). The focal plane detector of Xtend is the Soft X-ray Imager (SXI), which is back-illuminated, fully-depleted X-ray CCDs.<sup>10,11</sup> Xtend is designed to cover a large field of view ( $38' \times 38'$ ) with an angular resolution of  $< 1'.7$ . The required energy resolution is  $< 200$  eV at 6 keV, typical for X-ray CCD sensors.

SXI is composed of SXI-DE (Digital Electronics), SXI-PE (Pixel processing Electronics), SXI-S (sensor part), and SXI-CD (cooler driver). SXI-S consists of the FE (Front-end Electronics), video boards, four CCD chips installed on the cold plate, and 1ST (single-stage Stirling cooler). SXI-PE has two mission I/O (MIO) boards, and each runs two CCDs by generating CCD clocking patterns. Each CCD chip consists of two segments “AB” and “CD”, for which frame images are read out individually. The designed operating temperature of the CCDs is  $-110^{\circ}\text{C}$ . The CCDs are equipped with an optical blocking filter made of Al.<sup>12</sup> We have four observation modes of SXI, the full-window, 1/8-window, 0.1-s burst, and 1/8-window+burst modes. The frame cycle is 4 s for all the modes. The frame exposure is 3.96 s for the full-window mode, and is reduced to 0.46 s, 0.06 s, and 0.06 s for the 1/8-window, 0.1-s burst, and 1/8-window+burst modes, respectively. The two modes with a small imaging area (1/8-window and 1/8-window+burst) are intended for bright point-like sources, to avoid the pile-up of photons.<sup>13</sup> The 0.1-s burst mode is primarily for calibration purposes. To achieve the desired energy

---

E-mail: suzuki.hiromasa@jaxa.jp

resolution, we artificially inject charges into the imaging area.<sup>14–16</sup> We inject charges into every 160th physical row, which corresponds to 80th logical row after the on-chip  $2 \times 2$  binning.

## 2. INITIAL OPERATION PROCEDURE

### 2.1 Overview

We began operations to start up SXI on Oct. 17, 2023 (UT), 40 days after the launch. Table 1 summarizes our initial operation procedures. We turned on the electronics in the first four days, then started cooling of the CCDs. We spent about a month for optimization and verification of operation and observation parameters. SXI has been in the nominal operation phase from Feb. 2024, but we decided to make an additional adjustment of the charge-injection rows in Mar. 2024. We describe each procedure in the following subsections.

Table 1. Summary of the initial operations of SXI

Date and Time (UT)	Operation	Note
2023 Oct. 17 03:08	SXI-PE on	
2023 Oct. 17 03:09	SXI-DE on	
2023 Oct. 18 04:10	SXI-S-FE on	CCD temperature monitoring started
2023 Oct. 18 05:47	Video on	
2023 Oct. 18–19	CCD health check ( $\sim 0^\circ\text{C}$ )	Full-window mode verified
2023 Oct. 20 03:10	SXI-CD on	CCD heater control started
2023 Oct. 20 04:08	CCD cooling started	
2023 Oct. 21–22	CCD health check ( $-110^\circ\text{C}$ )	Full-window and 0.1-s burst modes verified
2023 Nov. 1–2	CCD health check ( $-110^\circ\text{C}$ )	1/8-window and 1/8-window+burst modes verified
2023 Nov. 1 21:31	1/8-window position adjusted	1/8-window mode
2023 Nov. 2 16:29	1/8-window position adjusted	1/8-window+burst mode
2023 Nov. 2 18:07 to Nov. 9 03:48	Observation interrupted	See Section 4.1
2023 Nov. 18 14:50	Bad columns masked	CCD3, Segment 2
2024 Mar. 10 06:27	Charge Injection rows adjusted	
2024 Mar. 10 06:26 to Mar. 11 00:51	Inappropriate dark level calculation	See Section 4.2

### 2.2 Starting up the electronics

Here we summarize the procedure of the start-up operations of the electronics, SXI-PE, SXI-DE, SXI-S-FE, and SXI-CD. Figure 1 shows the timeline chart of our operations starting from the startup of DE to the temperature stabilization of the CCDs at  $-110^\circ\text{C}$ . We confirmed that the current and power of each component were consistent with the values from on-ground tests when we turned on each. We note that the  $\approx 1.5$  hr variability of the current of the electronics seen in the top panel of Figure 1 is due to the variable spacecraft bus voltage, which depends on the satellite location and direction of the Sun. After the four FEs were turned on, the CCD temperature monitoring became available. Then we turned on the CD and started cooling of the CCDs.

### 2.3 CCD health check and countermeasure against “anomalous charge” problem

We confirmed the health of the CCDs by examining raw frame images. We tested the full-window mode before beginning the CCD temperature control, and all the four modes at  $-110^\circ\text{C}$ . Figure 2 shows in-orbit raw frame images at  $-110^\circ\text{C}$  obtained on Oct. 21, 2023, which are almost identical to those obtained on ground except for cosmic-ray induced events.

Because we sometimes experienced the “anomalous charge” problem\* in on-ground tests, we had to prepare a countermeasure procedure against it in case the problem appears in orbit as well. Figure 3 is the flow chart

\*Large amount of charges seem to be injected into the imaging area, making a large fraction of the pixels in a frame saturated with the pulse height of 4095 ch. The cause is yet to be identified. See Noda et al., SPIE, in prep.<sup>17</sup> for details.

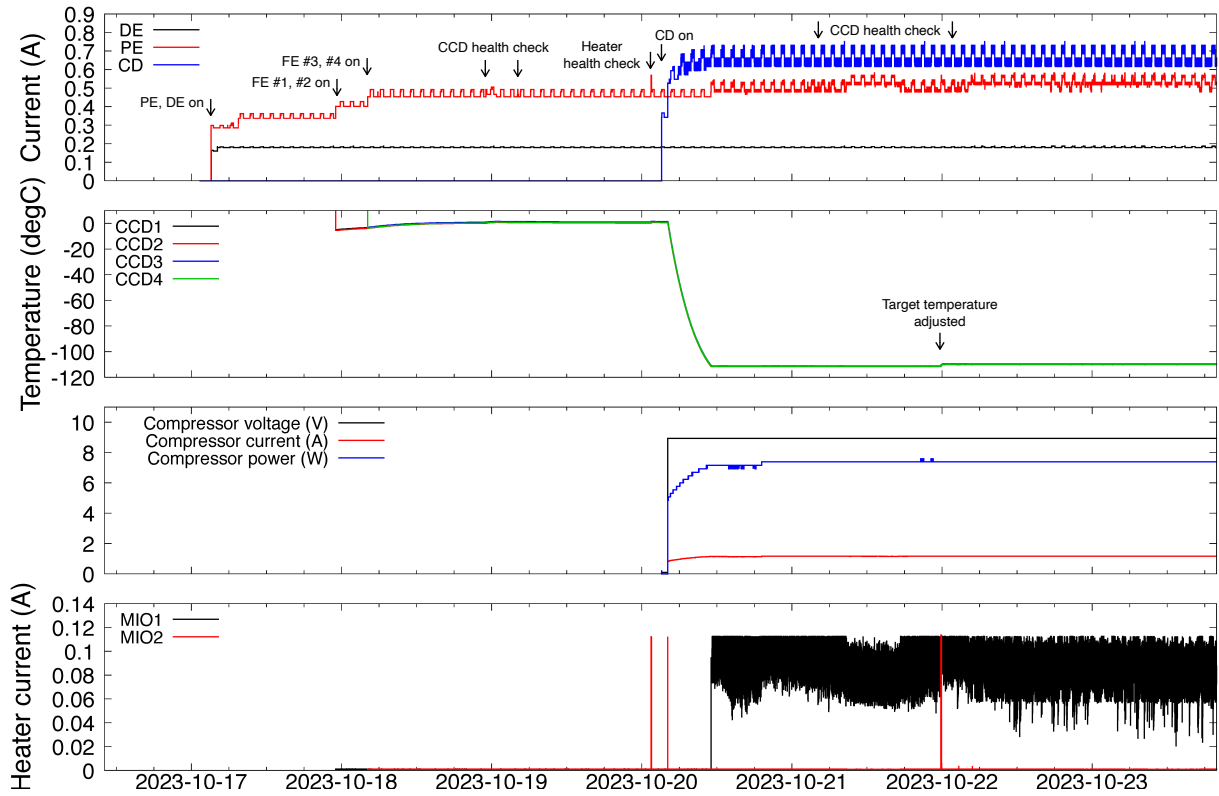


Figure 1. Timeline chart of the SXI house-keeping data related to the electronics and cooling system during the start-up operations.

of this procedure. We would have switched to the countermeasure clocking modes if the anomalous charges appeared in the raw frame images either before or after the temperature control started. Fortunately, in reality, we did not find any evidence for this problem in orbit.

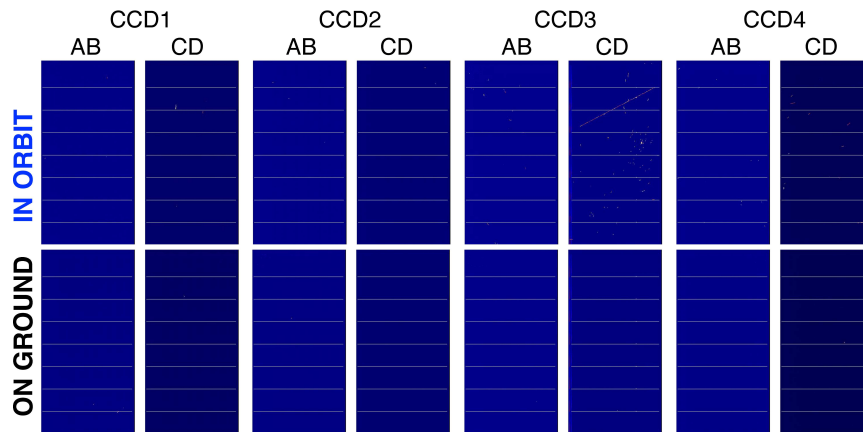


Figure 2. In-orbit raw frame images at  $-110^{\circ}\text{C}$  and a comparison with on-ground frames. The eight white rows in each frame are the charge-injection rows, where the pulse heights are saturated at 4095 ch. The color scale is the same for all the frames (0–4095 ch). The white dots and tracks seen in the in-orbit frame images are cosmic-ray induced events.

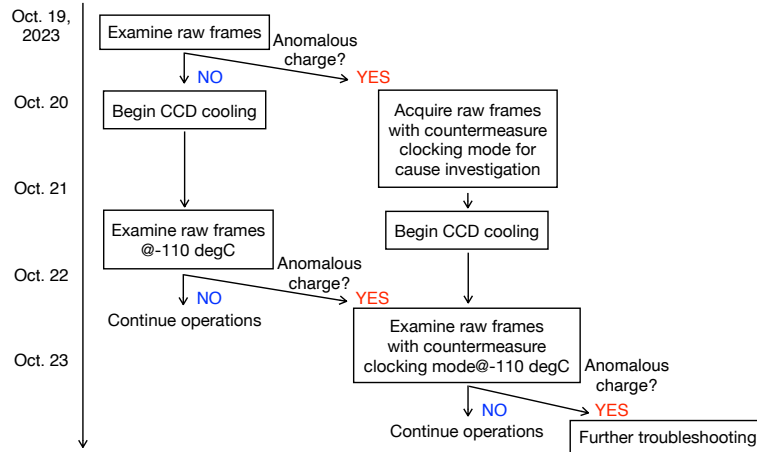


Figure 3. In-orbit operation procedure against the anomalous charge problem. In reality, we did not experience the anomalous charges, and thus we followed the simplest (leftmost) case.

## 2.4 Verification of the performance of CCD temperature control

The CCD temperature has been controlled since Oct. 20, 2023 (Figure 1). We confirmed the cooling performance of the 1ST and its stability. In combination with the two heaters attached to the cold plate, the cooling system successfully keeps the operating temperature of the CCDs,  $-110^{\circ}\text{C}$ . We note that the original target temperature ( $-111.3^{\circ}\text{C}$ ) was found to be slightly offset from the desired one, thus we adjusted it on Oct. 21. In Figure 1, one can see that only the heater of MIO1 is working mostly, indicating that the heater duty is  $\approx 50\%$ .

## 2.5 Verification of protection against South Atlantic Anomaly passages

In order to protect the CCDs from degrading due to enhanced radiation in the South Atlantic Anomaly (SAA) region, we stop the CCD clocking and application of the back-bias voltage during SAA passages. Following our original plan, we tried to make this operation automatic based on the satellite location. During our test of this automated operation starting from Nov. 9, 2023, however, we found that calculated SAA-in and out time was incorrect and thus the operations for protection were not working correctly, which later turned out to be due to a minor error in the orbit calculation. Therefore we decided not to use this function based on the satellite location, and rather issue time-set commands.

When the satellite leaves SAA, SXI-PE first runs a dedicated CCD clocking mode to wipe out stored charges in the imaging area during the SAA passage (CCD “erasing” mode) and then resumes the clocking for the nominal observations. Figure 4 shows pulse heights of 5.9 keV and 6.5 keV X-ray events from the onboard  $^{55}\text{Fe}$  calibration source as a function of time after SAA passages. The initial high pulse heights are probably due to the stored charges left even after the CCD erasing, but it was confirmed that the pulse heights become stable after  $\approx 200$  s.

## 2.6 Verification of dark-level calculation

To estimate pixel-dependent and time-variable dark levels, SXI-PE examines every frame and update the stored dark levels if the pulse heights meet certain criteria.<sup>10</sup> When the Xtend is looking at the day-earth rim, bright optical lights and albedo X-rays from the Earth make a lot of signals. This significantly affect the dark-level calculation of SXI-PE. Thus, we stop the dark-level calculation while uninterrupting observations during these periods.

In the nominal operations of SXI, dark levels are initialized regularly (nominally  $\approx$  once a day) in order to reset incorrect dark levels mainly caused by electronic crosstalk between two adjacent segments when a large amount of charges is generated by a charged particle (“cosmic-ray echo” event<sup>18</sup>). The negative signals as a result of the crosstalk cause an error in the dark-level calculation, resulting in generating persistent, low energy ( $\lesssim 1$  keV) events even without true X-ray inputs. In Figure 5, we show the effect of such incorrect dark levels

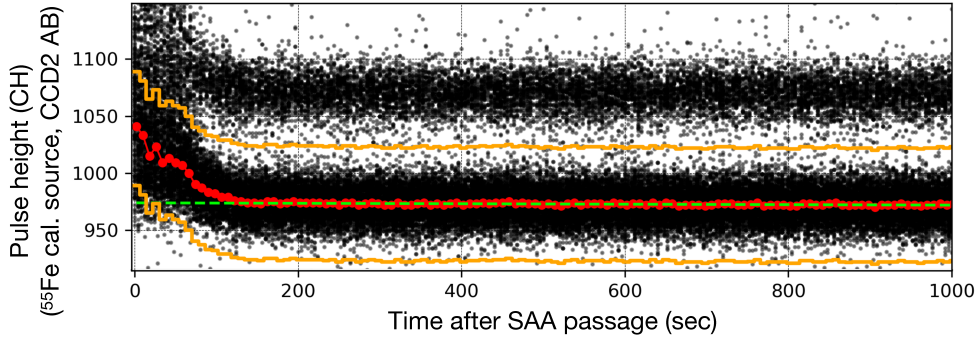


Figure 4. Behavior of pulse heights of Mn-K $\alpha$  and K $\beta$  X-ray events from the  $^{55}\text{Fe}$  calibration source after SAA passages. The black dots are X-ray events. The green dashed line indicates the average pulse height of Mn-K $\alpha$  in the stable period. The Mn-K $\alpha$  centroids at individual time bins, calculated from the data points enclosed with the orange lines, are shown in red.

and their initialization. The increasing low energy event rates, most prominent on Oct. 23, 2023, are mostly due to an increasing number of pixels with such incorrect dark levels. Such enhanced pseudo events should be suppressed because they put a load on the data recorder. When the dark levels are initialized, the event rates are evidently suppressed as expected. Note that the apparent “offset” in the event rates in the left panel of Figure 5 is due to bad columns, which persistently generate pseudo events.

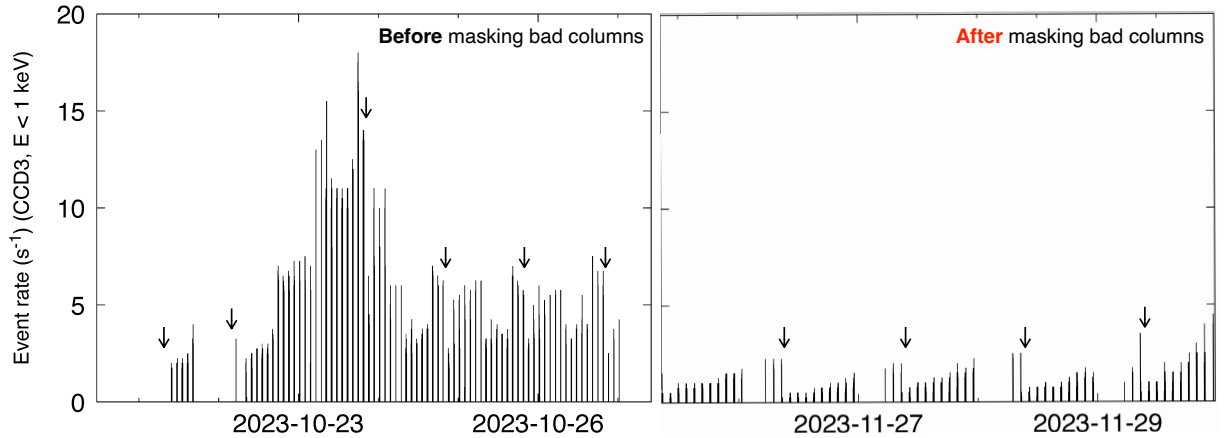


Figure 5. Event rate of CCD3 during night-earth observations before and after masking bad columns. The black arrows indicate time at which dark levels were initialized.

## 2.7 Optimization of the event selection algorithm

We collected basic imaging and spectral data needed for optimization of the event selection algorithm of all the four observation modes by Dec. 2023. Then we scrutinized the data to decide if we have to modify event selection parameters to optimize the imaging and spectroscopic performance of SXI. As a conclusion, we found that most parameters were appropriate and required no corrections. Examination of one of these parameters, the split threshold, is like presented in Figure 6. Increasing split threshold values result in degraded spectroscopic performance but more efficient event detection. The original value turned out to meet the requirements of the energy resolution and effective area. We made a minor update on the algorithm on the other hand, masking bad columns, to suppress unimportant events (Figure 5).

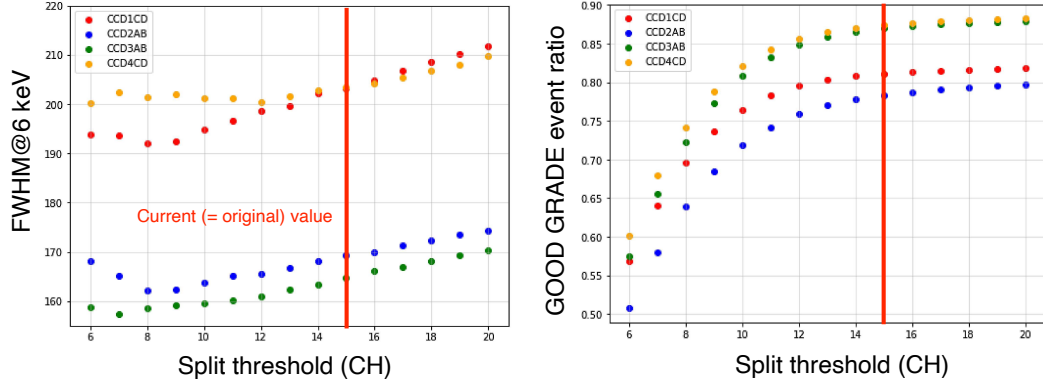


Figure 6. Split-threshold dependence of spectroscopic performance, the energy resolution (left) and good-grade event ratio (right). The red vertical lines are the original value of the split threshold determined before the launch, which was kept unchanged. The energy resolution in the left panel is less than the full performance<sup>7</sup> because we used data before the full processing.

## 2.8 Adjustment of the 1/8-window position

Adjustment of the aim point of XRISM was done for the other instrument, Resolve.<sup>19,20</sup> This slight correction was not important for Xtend given its large field of view in the case of the full-window and 0.1-s burst modes. On the other hand, it was our task to adjust the small window position for the 1/8-window and 1/8-window+burst modes. Based on the peak position of the diffuse celestial source Abel 2319, observed in Oct. 22–24, 2023, we determined the offset between the peak and central position of the original window region. The offset was found to be  $\approx 28$  arcsec. We then corrected the CCD clocking pattern for the 1/8-window and 1/8-window+burst modes to shift the window position, and tested them with our ground test system composed of EM (Engineering Model) CCDs before using them in orbit. The corrected window position was then verified with the observations of the point-like source NGC 4151 in Dec. 2–4, 2023 (Figure 7).



Figure 7. Point-source images obtained with the 1/8-window (left) and 1/8-window+burst (right) modes after the adjustment of the window position. The white and green boxes indicate the window regions before and after the adjustment, respectively.

## 2.9 Adjustment of the charge-injection rows

We officially moved to the nominal operation phase in Feb. 2024. However, we decided to make another special operation after that. In the full-window mode, one of the charge-injection rows overlaps the aim point (Figure 8 (a)). This results in  $\sim 10\%$  loss of photons for point-like sources. Weighing the effort and risk for an additional operation and the scientific merit of it, we decided to adjust the charge-injection rows in Mar. 2024, although this configuration already met all the requirements.

In a similar manner to the adjustment of the window position, we first modified the CCD clocking pattern to shift the charge-injection rows, then tested the modified clocking mode on ground. In this case, we also had to consider potential impact on the charge-transfer-inefficiency correction. So we accumulated data with

the ground test system to examine if this adjusted clocking mode had any unexpected impact and if we need to perform additional observations for calibration after performing this adjustment onboard. As a result, we confirmed that the original charge-transfer-inefficiency correction was still applicable to data with the adjusted clocking mode (Figure 8 (b)). Thus the spectroscopic performance should be unchanged. Confirmation with in-orbit observations is ongoing and will be reported by Uchida et al in prep.

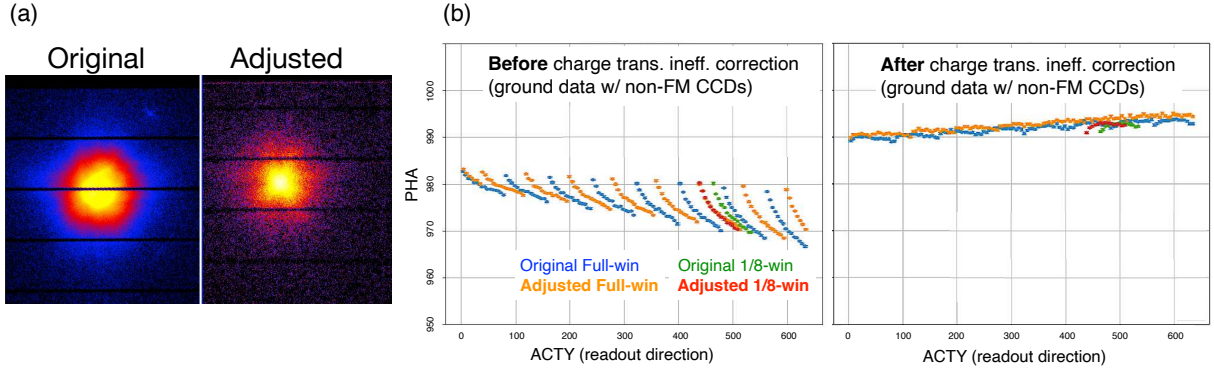


Figure 8. (a) Extended-source images before and after the charge-injection-row adjustment. The black rows without counts are the charge-injection rows. (b) 5.9 keV pulse height distribution along the readout direction before and after correction for charge transfer inefficiency. These are from on-ground experiments to confirm that the original charge-transfer-inefficiency correction algorithm is applicable to the data obtained after the adjustment of the charge injection rows.

### 3. CALIBRATION AND PERFORMANCE VERIFICATION PROCEDURE

Here we briefly summarize our calibration procedure, which is based on the pre-launch plan.<sup>21</sup> The calibration items and relevant data for SXI are listed in Table 2. For evaluation of the effective area, we observe point-like sources in coordination with other X-ray telescopes such as NuSTAR. For the detector response including detector gain and energy resolution, we need line emissions for which exact centroid energies are known. For this purpose, in addition to the onboard  $^{55}\text{Fe}$  calibration sources, we use well-studied supernova remnants and galaxy clusters. As for the quantum efficiency and contamination, we need to focus on the low energy part,  $\lesssim 1$  keV. We also need stable sources, thus low-temperature supernova remnants are one of the most suitable targets. We also use day-earth albedo X-rays, which are expected to be a spatially flat emission, to examine the pixel-to-pixel difference of the contamination. The timing accuracy can be evaluated with the Crab pulsar, for which the pulse period is well known. Note that we use X-rays detected during the frame transfer (out-of-time events) with the 0.1-s burst mode and reconstruct the pulse profile of Crab, thereby we can compare the pulse timing with other instruments (See Nakajima et al., 2018 for details<sup>18</sup>). As XRISM is a low-earth-orbit satellite, plenty of day- and night-earth observation data are available. The night-earth data represent pure non-X-ray background. The bright and uniform optical lights during day-earth observations can be used for evaluation of the optical blocking performance.

We already obtained basic data sets for all the calibration and performance verification items and data analysis is ongoing. The resultant performance will be presented by Uchida et al. in prep.

Table 2. Calibration items and relevant data for SXI

Calibration item	Data
Effective area	3C273, G21.5–0.9
Detector response	1E0102.2–7219, Perseus, N132D, Cygnus Loop, $^{55}\text{Fe}$ calibration sources
Quantum efficiency	1E0102.2–7219
Contamination	1E0102.2–7219, Day-earth data
Timing accuracy	Crab
Non-X-ray background level	Night-earth data
Optical blocking performance	Day-earth data

## 4. LESSONS LEARNED

### 4.1 Need for tests with a “test as you fly” environment

When we protect the CCDs against SAA passages, we send time-set commands to stop the CCD clocking, wait for a few seconds, and then stop the application of the back-bias voltage. At the time we first tested the 1/8-window mode on Nov. 1–2, 2023, commands to decrease the back-bias voltage were sometimes not accepted because the waiting time was not enough and the clocking was still running. We had tested these operations a lot of times on ground, but only a few times with the “test as you fly” setup, with the same series of the commands as the in-orbit operations. We had to interrupt observations until we resolved the cause and take measures (Table 1). After a series of our cause investigation, we confirmed that the time needed to stop the CCD clocking may sometimes exceed the original wait time. Therefore, we extended the wait time and resumed observations on Nov. 9.

### 4.2 Dark-level calculation

Keeping appropriate dark levels is quite important because wrong values lead to a large number of pseudo events as we described in Section 2.6. Thus, in our case, regular initialization of dark levels is essential, thereby we reset the cosmic-ray echo effect. The high event rates seen on Oct. 23, 2023 in Figure 5 is due to an inappropriate operation where we failed to initialize dark levels once a day.

The other lesson we learned about dark levels is that we should be careful about the status of the dark-level calculation when we perform special operations. On Mar. 10, 2024, when we adjusted the charge-injection rows, we ran the CCD erasing with the dark-level calculation enabled. This resulted in anomalous dark levels in Mar. 10–11 (Table 1).

## 5. SUMMARY

In this paper, we summarized the initial operation procedure of SXI, the focal plane detector of Xtend onboard XRISM. We started our operation on Oct. 17, 2023, 40 days after the launch. The CCDs have been kept at the designed operating temperature of  $-110^{\circ}\text{C}$  after the electronics and cooling system were successfully set up. We verified the observation procedure, stability of the cooling system, all the observation options with different imaging areas and/or timing resolutions, and operations for protection against SAA passages. We optimized the operation procedure and observation parameters including the cooler settings, window position for the small window modes, and event selection algorithm. We started observations for calibration and performance verification, the results of which will be presented by Uchida et al. in prep.

## ACKNOWLEDGMENTS

This work was supported by JSPS/MEXT KANENHI Nos. 21J00031, 22KJ3059, 24K17093, 19K21884, 20H01947, 20KK0071, 23K20239, 24K17105, 21H01095, 23K20850, 21K20372, 23K22536. This work was also supported by JSPS Core-to-Core Program (grant number: JPJSCCA20220002).

## REFERENCES

- [1] Tashiro, M. et al., “Concept of the X-ray Astronomy Recovery Mission,” **10699**, 1069922, International Society for Optics and Photonics, SPIE (2018).
- [2] Tashiro, M. et al., “Status of x-ray imaging and spectroscopy mission (XRISM),” **11444**, 1144422, International Society for Optics and Photonics, SPIE (2020).
- [3] Tashiro, M. et al., “Development and Operation Status of X-Ray Imaging and Spectroscopy Mission (XRISM),” **13093**, International Society for Optics and Photonics, SPIE (2024, in prep.).
- [4] Ishisaki, Y. et al., “Resolve Instrument on X-ray Astronomy Recovery Mission (XARM),” *Journal of Low Temperature Physics* **193**(5), 991–995 (2018).
- [5] Hayashida, K. et al., “Soft x-ray imaging telescope (Xtend) onboard X-ray Astronomy Recovery Mission (XARM),” **10699**, 1069923, International Society for Optics and Photonics, SPIE (2018).

- [6] Mori, K. et al., “Xtend, the soft x-ray imaging telescope for the X-Ray Imaging and Spectroscopy Mission (XRISM),” **12181**, 121811T, International Society for Optics and Photonics, SPIE (2022).
- [7] Mori, K. et al., “Status of Xtend telescope onboard X-Ray Imaging and Spectroscopy Mission (XRISM),” **13093**, International Society for Optics and Photonics, SPIE (2024, in prep.).
- [8] Hayashi, T. et al., “In-orbit performance of the XMA for XRISM/Resolve,” **13093**, International Society for Optics and Photonics, SPIE (2024, in prep.).
- [9] Tamura, K. et al., “In-orbit performance of the Xtend-XMA onboard XRISM,” **13093**, International Society for Optics and Photonics, SPIE (2024, in prep.).
- [10] Tanaka, T. et al., “Soft X-ray Imager aboard Hitomi (ASTRO-H),” *Journal of Astronomical Telescopes, Instruments, and Systems* **4**, 011211 (Jan. 2018).
- [11] Nakajima, H. et al., “Soft x-ray imager (SXI) for Xtend onboard X-Ray Imaging and Spectroscopy Mission (XRISM),” **11444**, 1144423, International Society for Optics and Photonics, SPIE (2020).
- [12] Uchida, H. et al., “Optical blocking performance of CCDs developed for the X-ray Astronomy Satellite XRISM,” *Nuclear Instruments and Methods in Physics Research Section A: Accelerators, Spectrometers, Detectors and Associated Equipment* **978**, 164374 (2020).
- [13] Yoneyama, T. et al., “Pile-up simulator for XRISM/Xtend,” **13093**, International Society for Optics and Photonics, SPIE (2024, in prep.).
- [14] Uchiyama, H. et al., “New CTI Correction Method for Spaced-Row Charge Injection of the Suzaku X-Ray Imaging Spectrometer,” *Publications of the Astronomical Society of Japan* **61**, S9–S15 (01 2009).
- [15] Nobukawa, K. K. et al., “Use of a charge-injection technique to improve performance of the Soft X-ray Imager aboard ASTRO-H,” *Nuclear Instruments and Methods in Physics Research Section A: Accelerators, Spectrometers, Detectors and Associated Equipment* **765**, 269–274 (2014). HSTD-9 2013 - Proceedings of the 9th International “Hiroshima” Symposium on Development and Application of Semiconductor Tracking Detectors.
- [16] Kanemaru, Y. et al., “Experimental studies on the charge transfer inefficiency of CCD developed for the soft X-ray imaging telescope Xtend aboard the XRISM satellite,” *Nuclear Instruments and Methods in Physics Research Section A: Accelerators, Spectrometers, Detectors and Associated Equipment* **984**, 164646 (2020).
- [17] Noda, H. et al., “New CCD Driving Technique to Suppress Anomalous Charge Intrusion from Outside the Imaging Area for Soft X-ray Imager of Xtend onboard XRISM,” **13093**, International Society for Optics and Photonics, SPIE (2024, in prep.).
- [18] Nakajima, H. et al., “In-orbit performance of the soft X-ray imaging system aboard Hitomi (ASTRO-H),” *Publications of the Astronomical Society of Japan* **70**, 21 (Mar. 2018).
- [19] Kanemaru, Y. et al., “Evaluation of the initial pointing accuracy of XRISM,” **13093**, International Society for Optics and Photonics, SPIE (2024, in prep.).
- [20] Maeda, Y. et al., “Initial in-orbit operation of the soft x-ray spectrometer Resolve onboard the XRISM satellite,” **13093**, International Society for Optics and Photonics, SPIE (2024, in prep.).
- [21] Miller, E. D. et al., “Planning in-flight calibration for XRISM,” **11444**, 1144426, International Society for Optics and Photonics, SPIE (2020).